Decarburization of Molten Fe–C Droplet: Numerical Simulation and Experimental Validation

Hyun-Jin CHO,[1] Sung-Hoon JUNG,[1] Sang-Joon KIM,[1] Hae-Geon LEE[1,2] and Youn-Bae KANG[1]*

1) Graduate Institute of Ferrous Technology (GIFT), Pohang University of Science and Technology (POSTECH), San 31, Hyoja-dong, Pohang, 790-784 Korea.
2) School of Engineering, Adama Science and Technology University, Adama, P.O. Box 5112 Ethiopia.

Decarburization of Fe–C droplet was investigated by fluid dynamics numerical simulation based on physical properties under gas phase mass transfer controlled regime. Fluid flow and species concentration fields around the droplet implementing a reaction of carbon with oxidant gas at the interface were calculated by a commercial CFD package which solves a set of transport equations. Overall decarburization rate of the molten Fe–C droplet was obtained by the simulation, and it was additionally validated by the present authors' own experiment using gas-liquid drop reaction in a levitation melting equipment. It was observed by the simulation that decarburization rate on the surface of a droplet was not homogeneous due to inhomogeneous gas distribution around the droplet. A new concept of local mass transfer coefficient ratio was proposed in the present study as a ratio of *effective* local mass transfer coefficient at a specific site over average mass transfer coefficient, as a function of θ (angle between direction of gas flow and direction to reaction site on the droplet surface from the droplet center) and dimensionless numbers regarding fluid flow:

$$\frac{k_g^{local}}{k_g^{average}} = f(\theta, Re_d, Sc)$$

Furthermore, effect of distance between two droplets was investigated by the present numerical model for decarburization of multiple droplets. The local mass transfer coefficient was found to have a significant impact on decarburization rate of a droplet when the other droplet locates very close. Relation between decarburization rate of two droplets and distance between them were analyzed.

KEY WORDS: decarburization; levitation; iron droplet; mass transfer; BOF.

1. Introduction

In a BOF (Basic Oxygen Furnace) steelmaking process, major portion of decarburization of hot metal is occurring at molten iron drops generated from molten steel bath. The droplets react either with oxidant gases in the BOF or with generated steelmaking slags in which significant amount of FeO$_x$ exist. When concern is given to the droplet decarburization by the oxidant gases, it is of importance to understand the phenomena of the decarburization and fluid flow behavior at the gas-liquid interface. Because of high-speed impinging jet onto a liquid iron bath surface, a large amount of iron droplets are generated and it increases the total interfacial area for the decarburization tremendously. Since the decarburization reaction is mainly affected by the interfacial area (surface of the droplets), it is necessary to understand the decarburization around the splashed droplets of liquid iron.

A number of experimental investigations on decarburiza-

tion characteristics of molten Fe–C alloys have been carried out by using a levitation melting technique,[1–5] and they reported the decarburization rate of iron droplets under different conditions (various oxidant gas, flow rate, reaction temperature controlled by temperature of droplets). Generally, in a BOF primary steelmaking process, the rate-controlling step of decarburization is known to be the mass transfer in the gas phase as long as C concentration in liquid iron is high.

It is well known that the mass transfer coefficient of gas component around a sphere is determined by several dimensionless correlations written as Eqs. (1) to (3).[5–7] Using those correlations, mass transfer coefficient of oxidant gas may be estimated, and consequently, decarburization rate of the iron droplet is calculated:

$$Sh = \frac{k_g d}{D_{ij}} = 2.0 + 0.6 Re_d^{1/2} Sc^{1/3} \quad {}^{6)} \quad \text{..............} (1)$$

$$Sh = \frac{k_g d}{D_{ij}} = 2.0 + 0.569 (Gr'Sc)^{0.25} + 0.347 Re_d^{0.62} Sc^{0.31} \quad {}^{7)} \quad \text{...} (2)$$

$$Sh = \frac{k_g d}{D_{ij}} = 2.0 + 0.569(Gr'Sc)^{0.25} + 0.533 Re_d^{0.62} Sc^{0.31 \; 5)} \; ... (3)$$

where Sh is the Sherwood Number, k_g is the mass transfer coefficient in the gas phase, d is the droplet diameter, D_{ij} is the binary diffusivity, Gr' is the mean Grashof number, Re_d is the Reynolds number ($= \rho_f u d / \mu_f$), Sc is the Schmidt number ($= \mu_f / \rho_f D_{ij,f}$). ρ, u, and μ stand for density, velocity, and viscosity, and the sub-index f refers to gas film near the droplet. Details of symbols used in the present study are listed in Nomenclature.

While the above correlations have been used widely, those are only applicable in a uniform gas flow and shape of the droplet is assumed to be spherical. If shape of the droplet is distorted due to strong turbulent flow, flow pattern around the droplet changes, and it would affect the relationship between the mass transfer coefficient and the dimensionless numbers. Besides, the phenomena that instantaneously occur at different local position on droplet surface are not considered since mass transfer coefficient obtained from the above correlations is an *averaged* value on an overall surface of droplet. In reality, the reaction extent of local surface of droplet has a wide difference. Simento *et al.* reported that the incoming oxidants are not likely to be uniformly distributed over the surface area on a flying droplet.[8] Nevertheless, until now, these correlations are the only way to estimate the mass transfer coefficient in a simple manner.

In order to understand the distribution of oxidant around an iron droplet and to determine decarburization reaction rate at the surface of droplet, a new approach has been attempted. Based on the above limitations, in the present study, a series of CFD (Computational Fluid Dynamics) simulation were carried out for analyzing the effect of convective flow characteristics at the local surface of the droplet. Moreover, the decarburization of more than a droplet generated and spread widely inside of steel bath was simulated. In this numerical approach, only the mass diffusivities of gas mixture around iron droplets were used by which it could be possible to estimate variation of mass transfer coefficient and consequently decarburization rate. This distinguishes the present approach from conventional approaches using a mass transfer coefficient for averaged reaction rate on an overall surface of droplet. Also, a series of experiments were carried out by using a levitation melting technique for a gas-liquid reaction in order to validate the numerical model. Furthermore, the influence of multiple droplets for decarburization rates as well as the distribution of local reaction extent was obtained by present investigation.

2. Numerical Model

2.1. Governing Equations

The decarburization reaction was numerically simulated on a single Fe–C droplet by implementing a chemical reaction model onto gas-liquid interface in multi-phase flows and by solving the governing equations in 2-dimensional axisymmetric system. The schematic of numerical domain is shown in **Fig. 1**. The governing equations are described for conservations of mass and momentum, volume fraction and
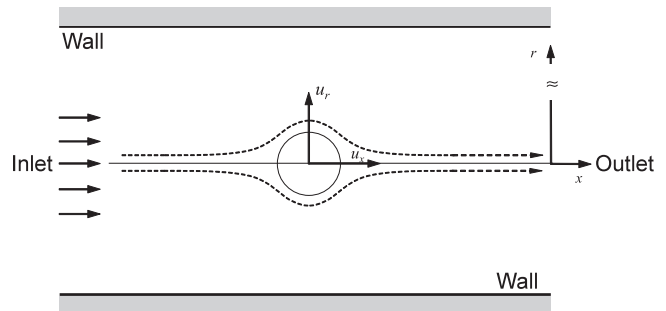

Fig. 1. Schematic of numerical domain for a single droplet.

conservation of chemical species, and are written as follows:
(1) Mass conservation

$$\frac{\partial \rho}{\partial t} + \frac{\partial}{\partial x}(\rho u_x) + \frac{\partial}{\partial r}(\rho u_r) + \frac{\rho u_r}{r} = 0 \; .... (4)$$

(2) Axial momentum conservation

$$\frac{\partial}{\partial t}(\rho u_x) + \frac{1}{r}\frac{\partial}{\partial x}(r \rho u_x u_x) + \frac{1}{r}\frac{\partial}{\partial r}(r \rho u_r u_x)$$
$$= -\frac{\partial p}{\partial x} + \frac{1}{r}\frac{\partial}{\partial x}\left[r\mu \left(2\frac{\partial u_x}{\partial x} \right) \right] + \frac{1}{r}\frac{\partial}{\partial x}\left[r\mu \left(\frac{\partial u_x}{\partial r} + \frac{\partial u_r}{\partial x} \right) \right] + F_x \; .... (5)$$

(3) Radial momentum conservation

$$\frac{\partial}{\partial t}(\rho u_r) + \frac{1}{r}\frac{\partial}{\partial x}(r \rho u_x u_r) + \frac{1}{r}\frac{\partial}{\partial r}(r \rho u_r u_r)$$
$$= -\frac{\partial p}{\partial r} + \frac{1}{r}\frac{\partial}{\partial x}\left[r\mu \left(\frac{\partial u_r}{\partial x} + \frac{\partial u_x}{\partial r} \right) \right]$$
$$+ \frac{1}{r}\frac{\partial}{\partial r}\left[r\mu \left(2\frac{\partial u_r}{\partial r} \right) \right] - 2\mu \frac{u_r}{r^2} + F_r \; .... (6)$$

(4) Volume fraction

$$\frac{1}{\rho^q}\left[\frac{\partial}{\partial t}(\alpha^q \rho^q) + \nabla \cdot (\alpha^q \rho^q \underline{u}^q) = \sum_{p=1}^{2}(\dot{m}_{pq} - \dot{m}_{qp}) \right] \; ... (7)$$

(5) Mass conservation equation of each species

$$\frac{\partial}{\partial t}(\rho^q \alpha^q Y_i^q) + \nabla \cdot (\rho^q \alpha^q \underline{u}^q Y_i^q) = -\nabla \cdot \alpha^q \underline{J}_i^q + R \; .... (8)$$

In the Eqs. (4)–(8), t is the time, u_x and u_r are the velocity in x and r directions, respectively, F_x and F_r are the external body force in the x and r directions and p is the pressure. For Eqs. (7) and (8), superscript q of $\alpha, \rho, \underline{u}$ refers to a phase q (in the present study, gas or liquid) where α is the volume fraction, ρ is the density and $\underline{u}$ is the velocity vector. $\dot{m}_{pq}$ is the mass transfer rate from a phase p to a phase q, Y_i^q is the mass fraction of each species i of the phase q, $\underline{J}_i^q$ is a mass flux of species i of a phase q, and R is the heterogeneous reaction rate.

In order to determine the heterogeneous reaction rate R, the following diffusive mass fluxes were considered as the decarburization rate since, in the present study, the rate-determining step of decarburization was assumed to the gas phase mass transfer:

$$R = -\rho^q \alpha^q D_{i,m} \delta_{CO_2,i} \frac{A_{interface}}{v^{cell}}\left(\frac{\partial Y_i^{q,diff}}{\partial x} + \frac{\partial Y_i^{q,diff}}{\partial r} \right) \; ... (9)$$

where $D_{i,m}$ is the mass diffusivity for species i in the mixture, $A_{\text{interface}}$ is the interfacial area between gas and iron droplet, v^{cell} is the volume of a cell in the numerical domain, $\delta_{CO_2,i}$ is the Krönecker delta and $Y_i^{q,diff}$ is the difference between Y_i^q and $Y_i^{q,equil.}$. The Krönecker is defined as:

$$\delta_{CO_2,i} = \begin{cases} 0 & \text{if } CO_2 \neq i \\ 1 & \text{if } CO_2 = i \end{cases} \quad \text{................(10)}$$

$Y_{CO_2}^{q,equil.}$ is the equilibrium mass fraction of species CO_2 for phase q at the surface of a droplet and it was computed by using equilibrium constant of decarburization reaction written as follows:[9]

$$\underline{C} + CO_2(g) = 2CO(g) \quad \text{.................(11)}$$
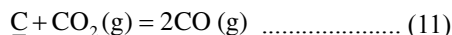
$$\ln\left(\frac{P_{CO}^2}{P_{CO_2} \cdot a_{\underline{C}}}\right) = -20\,327/T + 20.7 \quad \text{...........(12)}$$

where $a_{\underline{C}}$, P_{CO} and P_{CO_2} are the activity of dissolved carbon in the Fe–C droplet, the partial pressure of CO and the partial pressure of CO_2, respectively.

The mass diffusivity in the gas mixture, $D_{i,m}$, is computed as:[10]

$$D_{i,m} = \frac{1-X_i}{\sum_{j \neq i}\left(X_j / D_{ij}\right)} \quad \text{.................(13)}$$

where X_i is the mole fraction of species i.

The binary mass diffusivity of a component i with respect to a component j in the gas phase, D_{ij}, is determined by an equation proposed by Fuller, Schettler and Giddings's model as written in Eq. (14):[11]

$$D_{ij} = \frac{0.001T_f^{1.75}}{p\left(V_i^{1/3} + V_j^{1/3}\right)^2}\left(\frac{1}{M_i} + \frac{1}{M_j}\right)^{1/2} \quad \text{...........(14)}$$

where V_i and V_j are the diffusion volumes of molecules i and j, M_i and M_j are molecular weights, respectively. The diffusion volumes of gases shown in **Table 1** are provided by semi-empirical fit to available experimental data of diffusivities.[11] In **Table 2**, the diffusivities of binary mixtures used in the present simulation at different temperature are given. According to the Chapman-Enskog kinetic theory of gases,[12] the diffusivity may be proportional to temperature to the power of 1.5. However, experimental studies based on nearly 340 data asserted that the binary diffusivity is likely to be proportional to temperature to the power of 1.75.[11] In the present study, the suggestion of Fuller, Schettler and Giddings correlation was considered in order to define the binary mass diffusivity.[11]

2.2. Numerical Method

The computational domain was defined as shown in Fig. 1 and created in block-structured grid of approximately 54 000 (600×90) cells. The governing equations of unsteady state were solved by using the commercial CFD package Fluent®. Discretization was conducted by the PRESTO! scheme[13] for the pressure and a QUICK scheme[14] for the momentum and species transport. The solution of volume fraction was obtained by the Geo-Reconstruct algorithm[15] to track the interface between the gas and the iron droplet. The results obtained through the numerical method deliver results in a 3-dimensional space as the governing equations were solved in axisymmetric system. Obtained results were then presented in a 2-dimensional plane.

In the decarburization by CO_2 gas, initial weight of the droplet was set to 0.6 g and initial carbon content was 4.641 wt%, which is close to those used in the experiment (see Sec. 3). The inlet flow rate was varied from 0.5 to 5 L min^{-1} and the ratio of carbon dioxide to argon was varied from 0.05 to 0.2 as listed in **Table 3**. The calculations were continued until the carbon concentration reached 1.0 wt% above which the rate controlling step is evident to be the gas phase mass transfer control.[1,4,16–18]

3. Experimental

In order to confirm the validity of the numerical model, a series of experiments were also carried out in the present study for a decarburization of a Fe–C droplet by CO_2 containing gas. A conventional levitation melting technique was adopted. The power was supplied by a 30 kW, 260 kHz

Table 2. Binary mass diffusivities (D_{ij}).[11]

Binary mixture	Temperature (°C)	Diffusivity × 10⁴ (m² s⁻¹)
CO_2–Ar	1 650	1.531
CO_2–Ar	1 700	1.592
CO_2–Ar	1 750	1.654
CO_2–CO	1 650	1.612
CO_2–CO	1 700	1.676
CO_2–CO	1 750	1.741
CO_2–He	1 660	4.654
CO_2–CO	1 660	1.625

Table 3. Numerical and experimental conditions for decarburization in CO_2–Ar mixture.

Set No.	Initial temp. (°C)	%CO₂/ %Ar	Flow rate (L min⁻¹)	Initial weight (g)	Initial carbon composition (%)
1	1 650	10/90	1.0		
2	1 700	10/90	1.0		
3	1 750	10/90	1.0		
4	1 650	5/95	1.0		
5	1 650	20/80	1.0	0.6	4.641
6	1 650	10/90	0.5		
7	1 650	10/90	2.0		
8	1 650	10/90	5.0		

Table 1. Diffusion volumes of gases.[11]

Gas	Diffusion volume (m³ mol⁻¹)
CO_2	26.9
CO	18.9
Ar	16.1
He	2.88

high-frequency generator. The reaction chamber consisted of a quartz tube (OD: 20 mm, ID: 18 mm) and the upper part of the chamber was equipped with a gas inlet and an optical flat for viewing the upper surface of the molten droplet through a 45° prism as shown in **Fig. 2**. The lower end of the chamber was equipped with a copper mold and a gas outlet. The experimental temperatures varied from 1 650 to 1 750°C, and were controlled within ±10°C by adjusting the power control knob manually. Master alloys were prepared by melting electrolytic iron in a graphite crucible at 1 600°C in order to make the iron saturated by carbon. Small bars of 4 mm diameter were obtained using quartz sampling tube. Samples for the levitation melting were prepared by cutting and grinding the bar into smaller pieces whose weight was about 0.6 ± 0.01 g. The detailed experimental conditions are the same as numerical simulations as listed in Table 3. Ar gas used in the experiment was purified passing through a $CaSO_4$ column, and Mg chip at 450°C for dehydration and deoxidation. CO_2 gas was purified passing through a $CaSO_4$ column for dehydration.

The samples were introduced into the reaction chamber under a flow of the Ar gas. Once a sample was molten and reached predetermined experimental temperature, the experimental mixing gas was flown into the reaction chamber. After a determined reaction time, the power of the high-frequency generator was turned-off in order to quench the sample into water in the copper mold. Carbon content in the sample was analyzed by a C/S combustion analysis method.

4. Results

Figure 3 illustrates the contours of CO_2 and CO concentration (mole fraction) in the gas phase, and that of C concentration (mass fraction) in the droplet, which were obtained by numerical simulation of decarburization in CO_2–Ar mixture. The contours show the steep concentration gradient at the front interface of the droplet facing to inlet gas flow because of strong convective flow. On the other
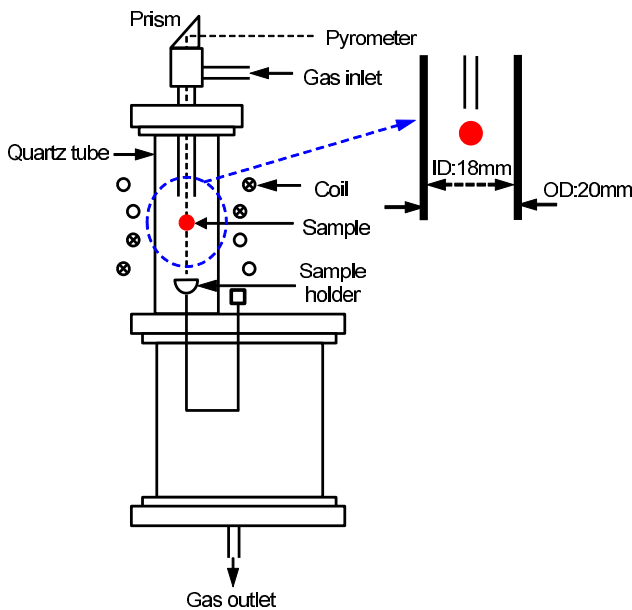
hand, less concentration gradient profile was observed at the rear interface facing to the way out of the flow.

From the numerical calculation results which provide C concentration at each cell at each time t (Y_C^{cell}), average C concentration in the droplet was computed by the Eq. (15) where C concentration in each cell was taken into account to obtain total mass of C (numerator), divided by whole mass of the droplet (denominator). Consequently, the averaged decarburization rate was obtained by dividing the average carbon concentration change by time interval as shown in Eq. (16):

$$Y_{C,average} = \frac{\sum_{i=1}^{n} Y_C^{cell} \rho^{cell} v^{cell}}{\sum_{i=1}^{n} \rho^{cell} v^{cell}} \quad \text{.................. (15)}$$

$$\text{Averaged Decarburization Rate} = \frac{\Delta Y_{C,average}}{\Delta t} \quad \text{.... (16)}$$

where $Y_{C,average}$ is the averaged mass fraction of carbon, Y_C^{cell} is the mass fraction of carbon in a cell i, ρ^{cell} is the density in a cell i, and i and n refer to an index of the cell and total number of the cells.

4.1. Effect of Gas Flow Rate

Under the gas phase mass transfer control regime, changing gas flow rate should affect the decarburization rate. In the case of various gas flow rate employed in the present study (from 0.5 to 5 L min^{-1}) at the fixed gas mixture ratio (P_{CO_2}/P_{Ar}), the changes of carbon concentration measured in the present experimental study are plotted in **Fig. 4** as symbols. The carbon concentration decreased linearly as the reaction time passed. Also the higher gas flow rate resulted
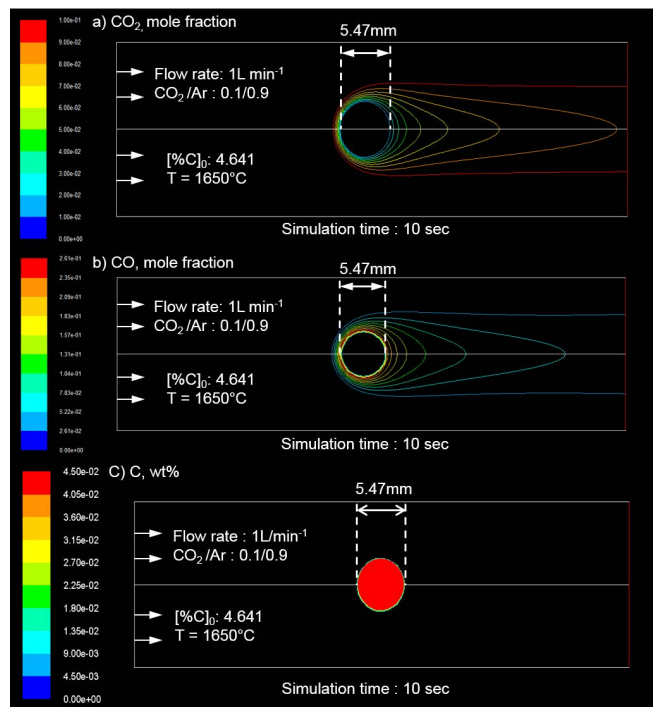
Fig. 3. Numerically simulated contours of CO_2 and CO mole fractions and mass percent of C for a single droplet. Initial C concentration is 4.641 wt%, temperature of the droplet is 1 650°C. Flow rate of the gas mixture ($P_{CO_2}/P_{Ar} = 1/9$) 1 L min^{-1}. (Online version in color.)
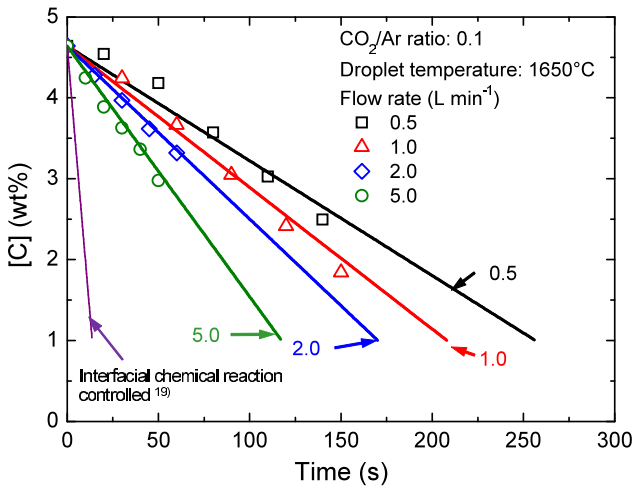
Fig. 2. Schematic diagram of experimental apparatus. (Online version in color.)

Fig. 4. Decarburization of Fe–C alloy droplets at 1 650°C under various gas flow rates. (Online version in color.)

Table 4. Numerical and experimental results of decarburization in CO₂–Ar mixture.

Set No.	Initial temp. (°C)	%CO₂/%Ar	Flow rate (L min⁻¹)	Numerical result (wt% s⁻¹)	Experimental result (wt% s⁻¹)
1	1 650	10/90	1.0	0.0175	0.0182
2	1 700	10/90	1.0	0.0186	0.0186
3	1 750	10/90	1.0	0.0196	0.0190
4	1 650	5/95	1.0	0.0089	0.0095
5	1 650	20/80	1.0	0.0337	0.0324
6	1 650	10/90	0.5	0.0142	0.0144
7	1 650	10/90	2.0	0.0214	0.0224
8	1 650	10/90	5.0	0.0310	0.0334

Fig. 5. Temperature dependence of the decarburization rate constant. (Online version in color.)

in the faster decarburization. This observation supports that the mass transfer in the liquid drop is not a rate-controlling step. The increased reaction rate by increasing the flow rate is due to the thinner effective boundary layer near the gas-liquid droplet interface and the steeper concentration gradient. The high gas flow rate increases the Reynolds number and it leads the large value of mass transfer coefficient according to the Eqs. (1)–(3).

If the rate-controlling step of the decarburization was the interfacial chemical reaction, the removal rate of carbon should have been estimated by the following equation for the reaction rate constant reported by Sain and Belton for very low S-containing Fe–C alloy:[19]

$$\ln k_f = -11\,700/T - 0.48 \quad \text{.................. (17)}$$

where k_f is the decarburization reaction rate constant in mol cm⁻² s⁻¹ atm⁻¹. The decarburization rate assuming the interfacial chemical reaction control regime was calculated and is also shown in the Fig. 4 as a thin line. It is seen that the calculated rate assuming the interfacial chemical reaction control regime is evidently faster than that of experimental data obtained in the present study. On the other hand, the numerical results obtained in the present study for each flow rate are shown as full thick lines in the same figure. The numerical simulation results are in very good agreement with the experimental data, and show linear decrease of the C concentration. Therefore, it is evident that the rate-determining step of decarburization at high carbon content is the gas phase mass transfer.

4.2. Dependence of Droplet Temperature

The numerical and experimental results of decarburization obtained at different temperatures in the present study are shown in **Table 4** (Set No. 1–3). The numerical calculations were carried out in the same condition as the experiments were carried out. As can be seen, the decarburization rates on the surface of droplets slightly increased as temperature of droplet increased. Since the binary mass diffusivity, D_{ij}, is a function of film temperature between gas and liquid droplet, increasing the droplet temperature increases the D_{ij} according to the Eq. (14), and subsequently increased the mass diffusivity in the gas mixture, $D_{i,m}$ as seen in the Eq.

(13), and diffusive mass flux in the gas phase. The results of numerical calculations have the same tendency for dependence of droplet temperature and accorded with experiment results. This also confirms that decarburization rate was controlled by the gas phase mass transport, and the rate could be accelerated by increasing the temperature which increases diffusion of gas components. **Figure 5** shows an Arrhenius-type plot of the rate constant, and the activation energy (E_A) extracted from the present experimental data is about 30 kJ mol⁻¹. By the numerical simulation, E_A was estimated to be about 50 kJ mol⁻¹. If the interfacial chemical reaction was the rate-determining step, the activation energy should be much larger than that of estimated value in the present study.[19] When the reduction of molten FeO by dissolved carbon in molten iron is considered, an overall reaction can be represented by Eq. (18):

$$\text{FeO}(l) + \underline{C} = \text{Fe}(l) + \text{CO}(g) \quad \text{................. (18)}$$

and the activation energy was reported by Sato *et al.*[20] as 184.1 kJ mol⁻¹, which is considerably higher than the value obtained in the present study. Therefore, these support that the gas phase mass transfer of reaction Eq. (11) is the rate-determining step in the present study.

4.3. Effect of CO₂ Partial Pressure

In order to observe the effect of partial pressure of CO₂

© 2014 ISIJ

in the gas mixture on the overall decarburization rate, the mole fraction of CO_2 in the inlet gas mixture (Ar + CO_2) was varied from 0.05 to 0.2 and the total gas pressure was maintained at 1 atm. The results of decarburization rate of several cases belonging to Set No. 1, 4 and 5 are shown in **Fig. 6**. Symbols are the measured carbon concentration while the lines are numerically calculated carbon concentration, at each gas mixture ratio. Similar to those shown in Fig. 4, the carbon concentration decreased linearly with the reaction time. This also confirms the gas phase mass transfer control of the decarburization. The decarburization rate at each gas mixture ratio was plotted as a function of P_{CO_2}/P_{Ar} in **Fig. 7**. The rate is proportional to the P_{CO_2}/P_{Ar} and this implies the decarburization of Fe–C droplets was controlled by gas phase mass transfer. Also, it is seen that the numerical calculations are in good agreement with the experimental data. This supports the validity of the numerical model developed in the present study.

Among the previous experimental investigations on the decarburization of molten Fe–C drops, that of Baker et al.[1] was chosen to validate the present numerical model inde-
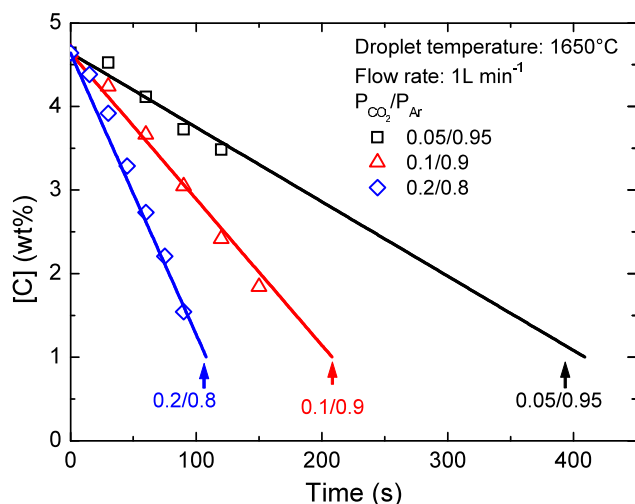
pendently, apart from the present authors' experiment. The reason to choose the work of Baker et al.[1] was that they provided with the clear statements of experimental dimension (quartz tube size and flow characteristics) which are essential to be used in numerical calculation. They investigated the decarburization kinetics in 0.7 g droplets of Fe–C alloy under using CO_2–He mixture gas at 1 660°C. The flow rate was 1 L min^{-1} and the CO_2/He ratio was varied from 0.01 to 0.5. All detailed experimental condition is given in **Table 5**. Calculation procedure was identical to the calculations shown previously. As can be seen in **Fig. 8**, the numerical calculation results are in good accordance with the experiment data of Baker et al.,[1] even though different gas mixture (CO_2–He) was considered.

5. Discussion

5.1. Inhomogeneous Decarburization Rate on the Surface of Droplet

The decarburization rates described in the previous sections were obtained from experimental approach and numerical approach, respectively. Those reaction rates were indeed *averaged* decarburization rates through the overall surface of droplets. Clearly, the rate obtained by the experimental approach should be the *averaged* one. This is because the decarburization rate was obtained by post-analysis of the carbon concentration in the droplet whose interior is thought to be homogenized. Therefore, the decarburization rate obtained by the experiment does not provide any information regarding different conditions of different decarburization reaction site. However, as seen in the Fig. 3, and as

Fig. 6. Decarburization of Fe–C alloy droplets at 1 650°C with changing gas mixture ratio (CO_2/Ar). (Online version in color.)
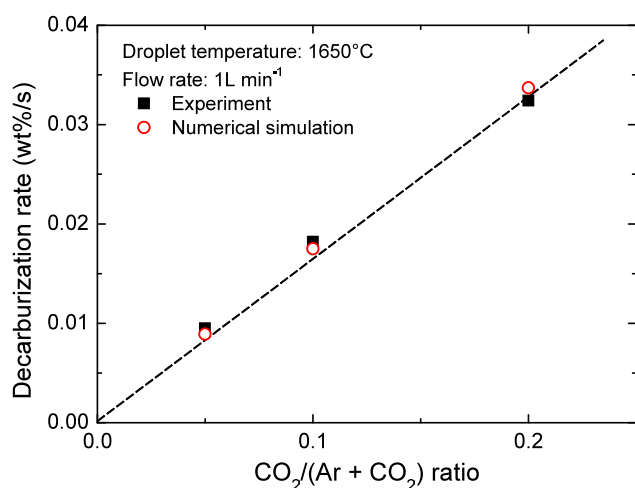
Table 5. Numerical and experimental conditions for decarburization in CO_2–He mixture.[1]

Set No.	Initial temp. (°C)	%CO_2/%He	Flow rate (L min^{-1})	Initial weight (g)	Initial carbon composition (%)
9		1/99			5.32
10	1 660	10/90	1.0	0.7	5.12
11		50/50			4.83

Fig. 7. Rate of decarburization in CO_2–Ar mixture at 1 650°C at flow rate 1 L min^{-1}. (Online version in color.)
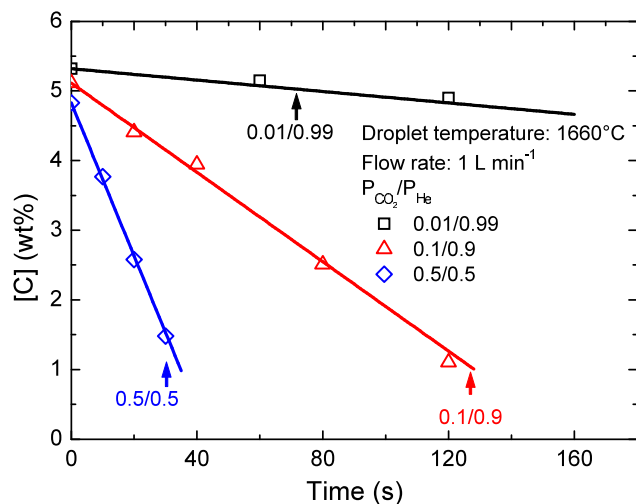
Fig. 8. Validation of the present numerical model using the experimental results by Baker et al.[1] (Online version in color.)

pointed out by Simento et al.,[8] there are differences of conditions for the decarburization. Concentration of oxidant such as CO_2 in the present study around the droplet is not homogeneous. Velocity and momentum of the gas are also different depending on the location. This should yield different mass transfer coefficient in the gas phase and different decarburization rate depending on the location around the droplet. Although the experimental approach was not able to reveal this, the numerical approach could provide the different decarburization behavior over the surface of the droplet. In the present study, it is termed as *local decarburization* characterized by θ, corresponding to an angle between direction of gas flow and direction to reaction site on the droplet surface from the droplet center. **Figure 9**(a) shows the local decarburization rates at the different position ($\theta = 30°$, $60°$, $120°$) on droplet surface by the present numerical calculations. These rates are seen to be almost invariant at the each location, regardless of the reaction time. It can be easily seen that the decarburization rate is high as the position is close to front interface of the droplet (θ approaches to $180°$). While the higher reaction rate is observed at the front interface facing to the incoming gas flow, the rear interface facing to the way out of the gas flow has the lower decarburization rate. The decarburization rates at the different flow rates can be seen in Fig. 9(b). When the gas flow rate is increased, the higher reaction rate is
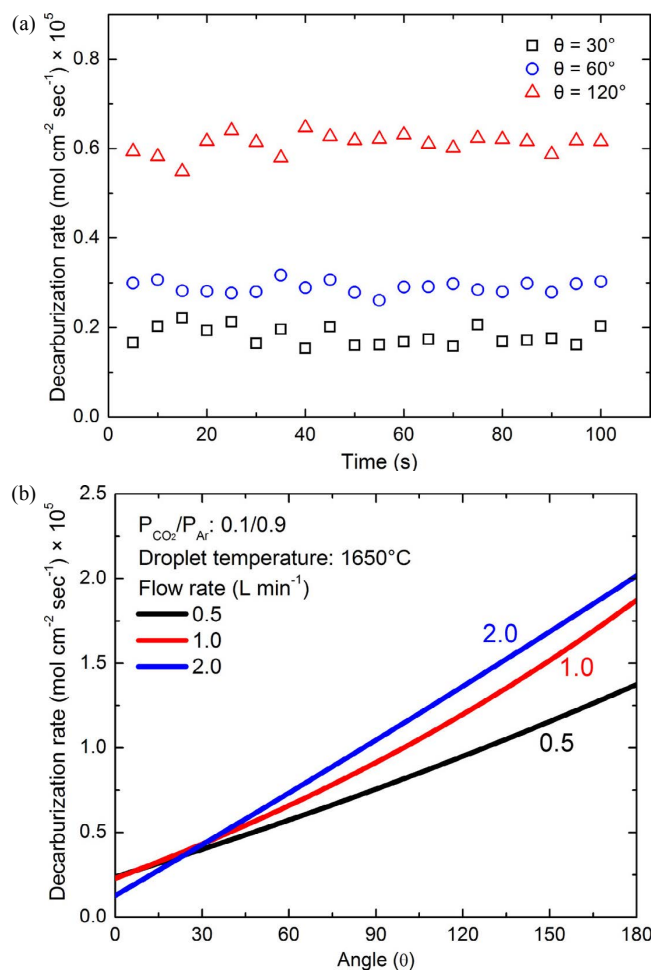
observed at the front interface of droplet due to steep concentration gradient and thinner boundary layer, on the other hand, the lower reaction rate is obtained at the rear interface since less amount of remaining oxidant gas produced the gentle concentration gradient and relatively thicker boundary layer. A comprehensive decarburization rate on a droplet is shown in **Fig. 10**. Figure 10 shows the decarburization rates of a droplet along a polar coordinate in two ways: one is the averaged decarburization rate shown as dashed line, and the other is the local decarburization rate shown as full line and short lines as error bars. The short lines with error bars represent the numerically calculated local decarburization rate at each location (θ) similar to those shown in Fig. 9. The full line is an estimated local decarburization rate connecting all numerically calculated values, as a function of θ. The dashed line represents overall decarburization rate of the droplet by averaging the local decarburization rate. This figure clearly shows that actual decarburization rate is not homogeneous but inhomogeneous depending on the location on the droplet surface under the same inlet flow characteristics. It means that, although the Fe–C droplet is exposed to an incoming gas containing certain fraction of oxidant gas (*i.e.*, $P_{CO_2}/P_{Ar} = 0.1/0.9$ in case of Fig. 10), actual decarburization rate is different on each location on the droplet surface under the same flow characteristics.

Since the decarburization rate depends on the location on the surface, characterized by θ and the flow characteristics, an effective local mass transfer coefficient k_g^{local} is defined in the present study by a local mass transfer coefficient ratio L_{kg}:

Local mass transfer coefficient ratio L_{kg}

$$\equiv \frac{k_g^{local}}{k_g^{average}} = f\left(\theta, Re_d, Sc\right) \quad \text{....... (19)}$$

where k_g^{local} is an effective gas phase mass transfer coefficient, taking into account of non-uniform gas flow characteristic and non-uniform concentration of the oxidant gas. It is a function of θ, Re_d, and Sc, since the effective local mass transfer coefficient is affected by gas flow behavior. By analyzing the numerical calculation results obtained in the present study under various flow condition, the local mass transfer coefficient ratio may be expressed by the following
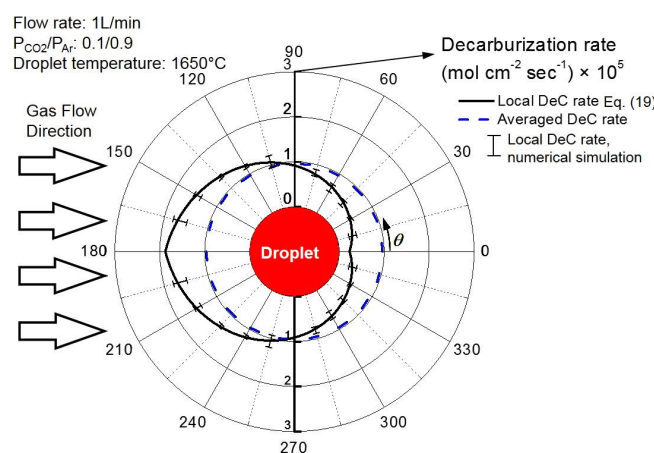

Fig. 9. Decarburization rate on the droplet surface: a) at different location, b) under different flow rate. (Online version in color.)

Fig. 10. Average and local decarburization rate on the surface of droplet. (Online version in color.)

form:

$$L_{kg} = 2.5 \exp\left\{\left(\frac{1}{2} - \left|\frac{1}{2} - \frac{\theta}{360}\right|\right)^A\right\} - B \quad (0 \le \theta < 360) \quad \dots (20)$$

for $Re < 25$

where

$$A = Re_d^{-0.15} Sc^{-0.64} \quad \dots\dots\dots\dots\dots\dots (21)$$

$$B = 1.5 \times \left(1 + 0.42 Re_d^{0.15} Sc^{0.1}\right) \quad \dots\dots\dots\dots (22)$$

When the gas is not blown onto the droplet, k_g^{local} should be identical $k_g^{average}$ since the radial diffusive flux only takes place. In the case of no convective gas flow, the Eq. (20) indicates that the value of local mass transfer coefficient ratio is 1 since the inside of exponential term becomes zero. If the convective gas flow should be considered, the effective local mass transfer coefficient is determined by using Eq. (20), in the absence of wake flow. **Figure 11** shows a comparison between the calculated local mass transfer coefficient ratio using the Eq. (20) and the ratio directly obtained by the numerical simulations. It can be seen that the expression given in the Eq. (20) can be used to represent the local mass transfer coefficient ratio. Moreover, using the Eq. (20) and a known overall (averaged) gas phase mass transfer coefficient, it is possible to calculate the effective local mass transfer coefficient for the accurate calculation of decarburization rate of a Fe–C droplet.

5.2. Evaluation of Overall (Averaged) Gas Phase Mass Transfer Coefficient

To evaluate the overall gas phase mass transfer coefficient obtained by the numerical simulation in the present study, it was further analyzed by comparing the mass transfer coefficient in the present study with those available in literature which can be obtained by the correlations given in Eqs. (1) to (3).[5–7] The latter was obtained by using dimensionless correlations written in Eqs. (1) to (3).[5–7] The former was calculated by using decarburization rate equation given in Eq. (23):

$$k_g = \left(-\frac{d\,\text{pct C}}{dt}\right) \Bigg/ \left\{\left(\frac{1\,200 A_s}{\rho_s V_s}\right)\left(\frac{1}{RT_f}\right) \ln\left(1 + p_{CO_2}^b\right)\right\} \dots (23)$$

where pct C is the average carbon concentration in the droplet obtained by the present numerical simulation, and $p_{CO_2}^b$ is the partial pressure of CO_2 in the bulk. All mass transfer coefficients were evaluated in the case of various gas flow rates at fixed gas mixture ratio (P_{CO_2}/P_{Ar}=0.1/0.9) and droplet temperature (1 650°C). The density and viscosity of gas mixture at the film temperature are 4.435×10^{-1} kg m^{-3} [21] and 5.47×10^{-5} kg m^{-1}s^{-1},[12,22] respectively. The value of gas diffusivity at the film temperature is 1.531×10^{-4} m^2 s^{-1} written in Table 2. **Figure 12** shows the overall (averaged) gas phase mass transfer coefficients as explained above. As shown in Fig. 12, the mass transfer coefficient values obtained from Eq. (23) using the simulated results are larger than those of Eq. (1).[6] This is because the Eq. (1) has no contribution of free convection. Besides, the influence of Reynolds number in Eq. (1) is relatively small compared with Eqs. (2) and (3) as the mass transfer coefficient is a function of $Re^{1/2}$. On the other hand, the mass transfer coefficients obtained from Eq. (23) using the simulated results are lower than values calculated from Eqs. (2) and (3). This is because of the strong contribution of forced convection in Eqs. (2) and (3). Reason of the discrepancy between mass transfer coefficient obtained from the numerical simulation and those from the correlations would be explained as the presence of wake flow behind the droplet. According to the study of Taneda,[23] when Reynolds number is lower than 24, the flow around the sphere is perfectly laminar. However, if Reynolds number is higher than 24, a vortex ring appears in the neighborhood of the rear stagnation point. In the presence of the wake flow, the outside oxidant gas not participating the decarburization reaction can be re-flown to the behind of droplet. It can be clearly explained that the decarburization rate is increased by existence of wake flow. While the correlations of Eqs. (2) and (3) were applicable to obtain the mass transfer coefficient for $Re > 24$, the conditions of present study have low Reynolds number range
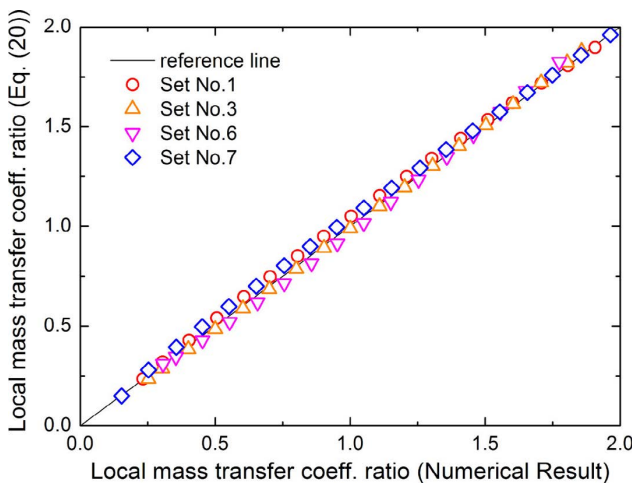

Fig. 11. Comparison of local mass transfer coefficient ratio between numerical results and Eq. (20). (Online version in color.)
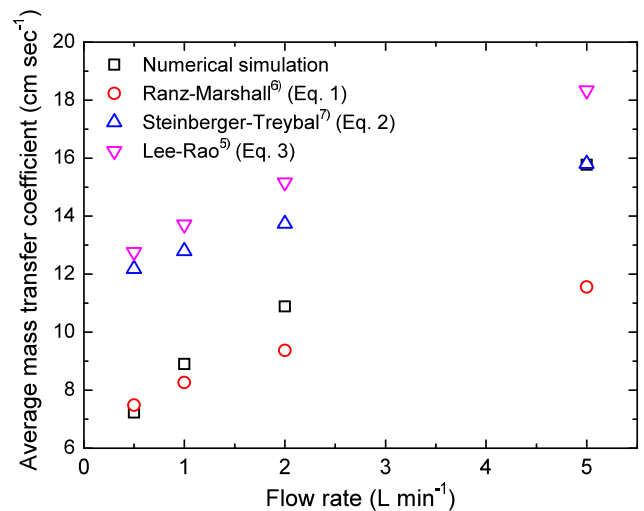

Fig. 12. Comparison of overall mass transfer coefficient obtained from numerical result and dimensionless correlations. (Online version in color.)
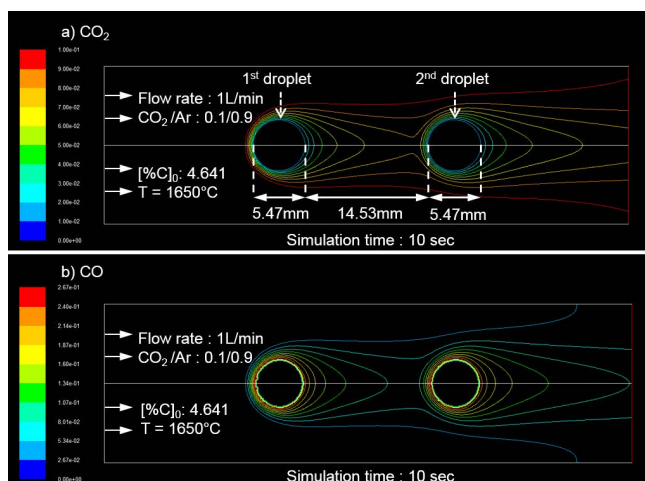
Fig. 13. Contours of CO_2 and CO mole fractions for multiple droplets. (Online version in color.)

Fig. 14. Ratio of decarburization rates between 2 droplets by numerical calculations. (Online version in color.)

(Re < 24). Since the wake flow can be found nowhere in the present study, the mass transfer coefficients estimated by the numerical simulation *via* the Eq. (3) is lower than the calculated values from Eqs. (2) and (3). In order to predict the more accurate mass transfer coefficient at the low Reynolds number, therefore, the correlation equations need to be modified for the low flow rate regime in the absence of wake flow, where Eqs. (2) and (3) are not applicable.

5.3. Multiple Droplets in an Oxidant Gas Flow

In real BOF steelmaking process, there are countless number of iron droplets flying in gas phase in the converter. It is very likely that one droplet reacts with the gas (composed of CO, CO_2, O_2, *etc.*) then a following droplet reacts with post-reacted gas. If it is assumed that those two droplets are moving in the same direction in the gas phase, they may be thought as two droplets aligned parallel to the incoming gas flow. The flow field around these two droplets may be different as the distance between these two droplets become short. In order to verify the influence of such gas flow field on the decarburization of the two droplets, the numerical calculation for decarburization of two droplets was carried out. The calculated results are shown in **Fig. 13** where the two droplets are physically separated 14.53 mm (rear interface of the 1st droplet to front interface of the 2nd droplet). It can be clearly seen that gas composition field around the 2nd droplet is different to the gas composition field around the 1st droplet. This should results in different decarburization rate between these two droplets. The difference of the decarburization rates was analyzed as a function of distance between the droplets. The initial gas flow rates were varied from 0.5 to 2 L min^{-1}, and the initial P_{CO_2}/P_{Ar} was set to 0.1. Since the 1st droplet placed at the left side prevents from the efficient supply of CO_2 gas to 2nd droplet, the CO_2 concentration is generally lower compared with that of a 1st droplet. **Figure 14** indicates the short distance between two droplets results in the large difference of the reaction rates. This difference becomes even larger as the flow rate increases. The difference between two decarburization rates diminishes as the distance between the two droplets increases as shown in the Fig. 14. In the present nu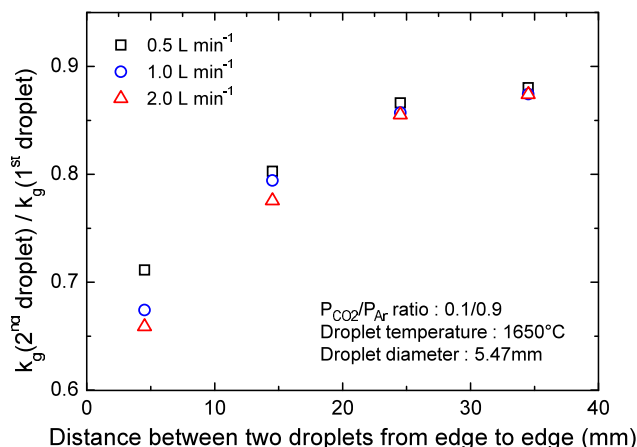merical calculations, the decarburization rates of two droplets almost converged when the distance was about 35 mm. This distance may be dependent on the temperature and gas composition. The results shown in the present study may be of use in the interpretation of decarburization phenomena for the case where many numbers of dispersed droplets exist inside the steelmaking vessel.

6. Conclusion

Decarburization phenomena under the various conditions on the Fe–C alloy droplets have been numerically and experimentally investigated in order to make a numerical simulation of decarburization process using CFD analysis more realistic.

(1) The rates of decarburization were obtained by solving a set of transport equations at oxidizing atmosphere. It was possible to predict the decarburization rate quantitatively and the validity of the numerical model was verified by the gas-liquid reaction experiments using a levitation melting equipment carried out by the present authors and that by Baker *et al.*[1] The results showed a good agreement with their experimental data, lending a strong support to the numerical model developed in the present study.

(2) Inhomogeneous of decarburization rate over the surface of droplet was analyzed, an effective local mass transfer coefficient for the decarburization reaction under gas phase mass transfer control regime was proposed. The ratio of the effective local mass transfer coefficient over averaged mass transfer coefficient was correlated to the location on the surface and flow characteristics. It means that the consideration of changeable flow behavior could be applied by numerical simulations.

(3) Decarburization in two splashed droplets which could be affected by continuously changing flow behavior in the BOF reaction vessel could be numerically simulated taking into account the changing flow behavior. This approach revealed that decarburizations of two adjacent droplets are not identical, and it depends on the distance between the two droplets. This may be further extended to multiple droplets in order to simulate accurate decarburization rate of each droplets suspended in the BOF reaction vessel.

Nomenclature

α: Volume fraction

α^q: Volume fraction for phase q

$A_{\text{interface}}$: Interfacial area between gas and steel phase [m^2]

A_s: Surface area of a specimen [m^2]

Δt: Time step of calculation [s]

$\delta_{\text{CO}_2,i}$: Krönecker delta

D_{ij}: Binary diffusivity [m^2 s^{-1}]

$D_{i,m}$: Mass diffusivity in the gas mixture [m^2 s^{-1}]

d: Diameter of liquid droplet [m]

F_x: External body force in x direction [N]

F_r: External body force in r direction [N]

Gr': Mean Grashof Number

θ: Angle of polar coordinate

$\underline{J}_i^q$: Mass flux of species i for phase q [kg m^{-2} s^{-1}]

k_f: Interfacial reaction rate constant [mol cm^{-2} s^{-1} atm^{-1}]

k_g: Mass transfer coefficient [m s^{-1}]

k_g^{local}: Local mass transfer coefficient [m s^{-1}]

k_g^{average}: Averaged mass transfer coefficient [m s^{-1}]

μ: Molecular viscosity [kg m^{-1} s^{-1}]

$\dot{m}_{pq}$: Mass transfer rate from phase p to q [kg m^{-3} s^{-1}]

ρ: Density [kg m^{-3}]

ρ^{cell}: Density in a cell [kg m^{-3}]

ρ^q: Density of phase q [kg m^{-3}]

ρ_s: Density of a specimen [kg m^{-3}]

p: Pressure [N m^{-2}]

$p_{\text{CO}_2}^b$: Partial pressure of CO_2

$\bar{R}$: Heterogeneous reaction rate [kg m^{-3} s^{-1}]

Re_d: Reynolds Number

r: Coordinate of radial direction

Sc: Schmidt Number

Sh: Sherwood Number

T_f: Film temperature [K]

u_x: Axial velocity component [m s^{-1}]

u_r: Radial velocity component [m s^{-1}]

$\underline{u}^q$: Velocity vector for phase q [m s^{-1}]

$\bar{V}_i$: Diffusion volume of species i [m^3 mol^{-1}]

V_s: Volume of a specimen [m^3]

v^{cell}: Volume of a cell [m^3]

X_i: Mole fraction of species i

x: Coordinate of axial direction

Y_i^q: Mass fraction of species i for phase q

$Y_i^{q,equil.}$: Equilibrium mass fraction of species i for phase q

$Y_i^{q,diff}$: Mass fraction difference of species i between Y_i^q and $Y_i^{q,equil.}$

$Y_{C,average}$: Averaged mass fraction of carbon

Y_C^{cell}: Mass fraction of carbon in a cell

REFERENCES

1) L. A. Baker, N. A. Warner and A. E. Jenkins: *Trans. Met. Soc. AIME*, **230** (1964), 1228.
2) L. A. Baker, N. A. Warner and A. E. Jenkins: *Trans. Met. Soc. AIME*, **239** (1967), 857.
3) P. A. Distin, G. D. Hallet and F. D. Richardson: *J. Iron. Steel Inst.*, **206** (1968), 821.
4) D. Widlund, D. S. Sarma and P. G. Jonsson: *ISIJ Int.*, **46** (2006), 1149.
5) H. G. Lee and Y. K. Rao: *Metall. Trans. B*, **13** (1982), 411.
6) W. E. Ranz and W. R. Marshall: *Chem. Eng. Prog.*, **48** (1952), 173.
7) R. L. Steinberger and R. E. Treybal: *AIChE J.*, **6** (1960), 227.
8) N. J. Simento, P. C. Hayes and H. G. Lee: *ISIJ Int.*, **38** (1998), 690.
9) D. R. Stull and H. Prophet: JANAF Thermochemical Tables, 2nd ed., NSRDS-NBS 37, US Department of Commerce, Washington, DC, (1971).
10) F. A. Williams: Combustion Theory, 2nd ed., Addison-Wesley, New York, NY, (1985), 625.
11) E. N. Fuller, P. D. Schettler and J. C. Giddings: *Ind. Eng. Chem.*, **58** (1966), 18.
12) S. Chapman and T. G. Cowling: The Mathematical Theory of Non-Uniform Gases, 3rd ed., Cambridge University Press, Cambridge, UK, (1970), Chapters 10 and 14.
13) FLUENT 12.0 Theory Guide, Ansys Inc., Canonsburg, PA, (2009).
14) B. P. Leonard: *Comput. Method. Appl. Mech. Eng.*, **19** (1979), 59.
15) D. L. Youngs: Numerical Methods for Fluid Dynamics, Academic Press, New York, NY, (1982), 41.
16) D. N. Ghosh: *Ironmaking Steelmaking*, **1** (1975), 36.
17) D. N. Ghosh: *Ironmaking Steelmaking*, **1** (1975), 45.
18) R. J. Fruehan and L. J. Martonik: *Metall. Trans. B*, **5** (1974), 1027.
19) D. R. Sain and G. R. Belton: *Metall. Trans. B*, **7** (1976), 235.
20) A. Sato, G. Aragane, K. Kamihira and S. Yoshimatsu: *Trans. Iron Steel Inst. Jpn.*, **27** (1987), 789.
21) F. P. Incropera and D. P. DeWitt: Fundamentals of Heat and Mass Transfer, 5th ed., John Wiley & Sons, Hoboken, NJ, (2001).
22) C. R. Wilke: *J. Chem. Phys.*, **18** (1950), 517.
23) S. Taneda: *J. Phys. Soc. Jpn.*, **11** (1956), 1104.